



# Zirconium-based Metal-Organic Frameworks for highly efficient solar light-driven photoelectrocatalytic disinfection

Laura Valenzuela<sup>1,\*</sup>, Georgiana Amariei<sup>2</sup>, Chizoba I. Ezugwu<sup>1</sup>, Marisol Faraldos<sup>3</sup>, Ana Bahamonde<sup>3</sup>, Marta E.G. Mosquera<sup>4</sup> and Roberto Rosal<sup>1</sup>

<sup>1</sup>Department of Chemical Engineering, Universidad de Alcalá, 28805 Alcalá de Henares, Madrid, Spain

<sup>2</sup>Department of Biological and Chemical Engineering-Process and Materials Engineering, Aarhus University, Denmark

<sup>3</sup>Instituto de Catálisis y Petroleoquímica, ICP-CSIC, Marie Curie 2, 28049 Madrid, Spain

<sup>4</sup>Department of Organic and Inorganic Chemistry, Institute of Chemical Research Andrés M. del Río (IQAR), Universidad de Alcalá, 28805 Alcalá de Henares, Madrid, Spain

## Abstract

Two synthesized zirconium-based Metal-Organic Frameworks (Zr-MOFs), using 2,6-naphthalenedicarboxylic acid (NDC) and amino-functionalized NDC (4,8-diaminonaphthalene-2,6-dicarboxylic acid, NDC-2NH<sub>2</sub>) as linkers, have been studied in photoelectrocatalytic disinfection processes. The Zr-based MOFs were deposited onto graphite paper and were deeply analysed to unravel their behaviour in electrocatalytic (EC), photocatalytic (PC) and photoelectrocatalytic (PEC) configurations under solar (Xe-arc lamp), visible (Xe-arc lamp + 400 nm cut-off filter) and 365 nm UV-LED irradiation. TPC results showed reproducible photocurrent response upon repeated on-off cycles and bandgaps were calculated to be 3.13 and 2.11 eV for Zr-NDC and Zr-NDC-2NH<sub>2</sub>, respectively. The highest photocurrent was obtained for 365 nm UVA in Zr-NDC and was similar for both UVA and solar irradiation in the case of Zr-NDC-2NH<sub>2</sub>. The Zr-MOFs catalytic electrodes were evaluated for their disinfection activity using a strain of *Staphylococcus aureus* and performance tracked by measuring colony forming units (CFU). The disinfection efficiency was higher in PEC than PC studies (>2-log reduction or 99% CFU inhibition) under 365 nm UVA irradiation, suggesting that the anodic bias potential effectively minimized the recombination of the photogenerated electron-hole pairs. A complete disinfection was reached after 60 and 20 min under irradiation of full Xe-arc (solar) spectrum in PC and PEC runs, respectively, for both Zr-MOFs. The high disinfection capacity under solar irradiation was attributed to the transfer of photoexcited electrons from ligand to cluster by high energy photons.

## 1. Introduction

Microbial contamination is a challenging concern due to the health threat caused by infections and the outspreading of bacterial resistance to antibiotics [1-3]. Conventional disinfection methods, like biocide chemicals or ultraviolet irradiation, have numerous shortcomings that may include the generation of disinfection by-products, high energy consumption, resistance to disinfectants and insufficient residual effect [4, 5]. Although UV-assisted disinfection does not lead to halogenated by-products, constituting an appealing alternative to chlorination, its major shortcoming is the lack of remnant effect [6]. It has been reported that some antibiotic resistant bacteria can survive upon UV treatment and be reactivated in the darkness [7]. Regarding H<sub>2</sub>O<sub>2</sub> disinfection, a powerful oxidant that decomposes in oxygen and

water also avoiding by-products generation, the main disadvantage lies in the additional costs and hazards arising from its transport, storage and handling [8]. Therefore, the development of high-performance and environmentally friendly techniques for the removal of pathogenic microorganisms (e.g., bacteria, viruses, fungi, etc.) is a growing demand [9]. Photocatalysis is regarded as a promising and efficient alternative for the inactivation of a wide range of pathogens in water, air or on surfaces because of its high oxidative capability, and the fact that it is a sustainable and cost-effective method that do not lead to released chemicals [10-13]. In the photocatalytic disinfection process, light irradiation triggers the generation of electrons and holes on the catalyst surface that give rise to a variety of reactive oxygen species (ROS) like hydrogen peroxide, superoxide and hydroxyl radicals, which are known to impair microorganisms by damaging cellular components including lipids, proteins and DNA [14, 15]. Nevertheless, the practical application of photocatalysis is generally limited by the fast recombination of photogenerated electron-

\* Corresponding author: laura.valenzuela@uah.es  
Available online: December 23, 2021

hole pairs. Photoelectrocatalytic processes attempt to overcome this constraint by immobilizing the photocatalyst on an electrically conducting support to which a bias potential is applied while irradiating, thus continuously extracting photoexcited electrons and increasing their lifetime [16-18]. In electrochemically assisted photocatalytic disinfection numerous strong oxidants including  $\text{H}_2\text{O}_2$  (e. g., active chlorine, active bromine,  $\text{O}_3$ ,  $\text{SO}_4^{\cdot-}$ , and  $\text{HO}\cdot$ ) can be in situ generated and inactivate pathogens in the bulk solution, adding to the direct oxidation at the electrode surface and overcoming the above limitations concerning insufficient residual effect and reagents handling [19]. Furthermore, it has been shown that the optimal applied potential in photoelectrocatalysis is lower than that required in electrocatalytic processes, thus reducing the energy consumption of the disinfection treatment [20].

Although wide band gap semiconductor materials such as  $\text{TiO}_2$  or  $\text{ZnO}$  have been extensively used as photoanodes, their activity is restricted to the UV region, which only accounts for 3-5% of the total solar spectrum [21,22]. Consequently, the exploration of efficient and stable solar light-driven photocatalysts is urgently needed [23-25]. MOFs are porous crystalline inorganic-organic hybrid materials consisting of metal ions or clusters interconnected through organic linkers. The photogeneration of electron-hole pairs in MOFs has been evidenced, along with their ability to oxidize or reduce different compounds [26,27]. MOF-based photocatalysts undergo a charge separation process similarly to inorganic semiconductors under light irradiation, so that photoinduced electrons migrate from the photoexcited organic linkers to the adjacent metal-oxo clusters (ligand-to-cluster charge transfer, LCCT) [28-30]. The most competitive advantage of MOFs over classical metal oxide semiconductors is their high tunability derived from the broad range of possibilities in the combination between metallic nodes and organic linkers [23,31]. As the energy required to induce the LCCT transition depends on the level of conjugation of the aromatic system in the ligand and the metal, MOFs offer the opportunity to optimize the photocatalytic activity at the molecular level, as well as the absorption wavelength range, by engineering the organic linker or by using mixed-metal clusters or/and mixed-linkers [32,33]. Thereby, ligands in MOFs can be replaced or functionalized allowing an effective utilization of solar energy with a subsequent enhancement of their photocatalytic performance [34,35]. Other advantages of using MOFs as photocatalysts are their extremely large surface area and high porosity providing more active sites and extra pathways for the migration of photoinduced

electrons, thus facilitating charge carrier separation [36,37]. The feasibility of MOFs as photocatalysts in environmental applications depends on their chemical stability [38]. Zirconium-based MOFs are becoming competitive catalysts for water treatment owing to their outstanding electronic properties and high chemical stability derived from the strong coulombic interaction between oxophilic  $\text{Zr}^{4+}$  and negatively charged termini of linkers [39-41].

In this work, two Zr-based MOFs were synthesized using naphthalene-2,6-dicarboxylic acid (NDC) and  $\text{NH}_2$ -functionalized NDC (4,8-diaminonaphthalene-2,6-dicarboxylic acid, NDC-2 $\text{NH}_2$ ) as organic linkers, and evaluated for their photoelectrocatalytic disinfection performance. Disinfection experiments used the gram-positive pathogenic bacterium *S. aureus* in electrocatalytic, photocatalytic and photoelectrocatalytic conditions under solar, visible and 365 nm UVA light irradiation. To the best of our knowledge, both Zr-NDC-2 $\text{NH}_2$  synthesis and the photoelectrocatalytic activity of these two Zr-MOFs are reported for the first time in the present study. This work offers new insights into the applicability of Zr-based MOFs for solar light-driven disinfection processes.

## 2. Materials and methods

### 2.1 Synthetic procedure for Zr-NDC and Zr-NDC-2 $\text{NH}_2$

A mixture of  $\text{ZrCl}_4$  (69.9 mg, 0.3 mmol), naphthalene-2,6-dicarboxylic acid (NDC, 64.86 mg, 0.3 mmol), benzoic acid (549.55 mg, 4.5 mmol, 15 equiv. with respect to the ligand) and  $\text{H}_2\text{O}$  (21.68  $\mu\text{L}$ ) in 10 mL *N,N*-Dimethylformamide (DMF) was stirred for 1 h. The resultant solution was then transferred to a 45 mL Teflon-lined stainless-steel autoclave followed by heating at 120 °C for 48 h under autogenous pressure. The product was collected by filtration, washed with DMF and  $\text{CH}_3\text{OH}$ . The purified product was dried at 100 °C for 12 h. The obtained sample was denoted as Zr-NDC. Similar synthetic procedure was employed to prepare Zr-NDC-2 $\text{NH}_2$  except that the ligand naphthalene-2,6-dicarboxylic acid was replaced by 4,8-diaminonaphthalene-2,6-dicarboxylic (NDC-2 $\text{NH}_2$ , 72.67 mg, 0.3 mmol) and the double amount of benzoic acid (1099.1 mg, 9 mmol, 30 equiv.) was used.

The crystalline structure of the as-synthesized MOFs was assessed by X-ray diffraction (XRD, X'Pert PRO, PANalytical) with  $\text{Cu K}\alpha$  radiation. The chemical stability of the photocatalysts was evaluated by contacting the material with ultrapure water at 37 °C for 24 h and, subsequently, quantifying soluble Zr(IV) ions by Inductively Coupled Plasma Atomic

Emission Spectroscopy (ICP-AES, PlasmaQuant® PQ 9000, Analytik Jena). Fourier transform infrared spectroscopy (FTIR, JASCO FT/IR-4600 spectrometer) was used to characterize the functional groups of the Zr-based MOFs in the 400–4000  $\text{cm}^{-1}$  range. UV–vis Diffuse Reflectance Spectroscopy (DRS) of the powder samples were collected on an Agilent Cary 5000 spectrophotometer and band gap values were determined using Planck-Einstein relation. The Photoluminescence (PL) properties were measured on solid samples using a LS50B Perkin Elmer luminescence spectrometer at room temperature.

## 2.2 Preparation and characterization of MOF-based electrodes

MOF-based working electrodes were fabricated by spray-coating using a nozzle regulated airbrush (Elite Q5). Briefly, 0.1 mL of a 10  $\text{g L}^{-1}$  suspension of the catalysts in ethanol were deposited onto sanded and prewashed GP substrates (SIGRACELL® PV15, SGL Carbon). The procedure was repeated ten times, achieving a mass surface density of 1.04  $\text{mg cm}^{-2}$ . Finally, the coated substrates were dried at 50 °C overnight. Surface morphology of the photocatalytic films was investigated by Scanning Electron Microscopy (SEM, Zeiss DSM 950) at an accelerating voltage of 25 kV after gold coating.

The photoelectrochemical properties of the MOF-based photoanodes were studied by Linear Sweep Voltammetry (LSV) and Transient Photocurrent (TPC) in the three-electrode cell configuration shown in Fig. 1. LSV was recorded at a scan rate of 5  $\text{mV s}^{-1}$  in the absence and presence of light irradiation and TPC was performed at +1.0 V vs. Ag/AgCl with 50 s light on and 50 s off cycles using a Metrohm Autolab PGSTAT101. Ten consecutive LSV scans were conducted with the same electrode, five in the dark and five in the presence of light irradiation.

## 2.3 Disinfection experiments and bioanalytical procedures

The inactivation experiments of the gram-positive bacterium *S. aureus* (CECT 240) were carried out using the same three-electrode system reported for the photoelectrochemical characterization. The microorganisms were first re-activated in NB (Nutrient Broth, 5  $\text{g L}^{-1}$  beef extract, 10  $\text{g L}^{-1}$  peptone, 5  $\text{g L}^{-1}$  NaCl, at pH 7) while shaking at 37 °C. For each disinfection run, fresh inoculum was added into the electrolyte under magnetic stirring, reaching an initial bacterial density of 108 cells  $\text{mL}^{-1}$ . Although Zr-NDC has been reported to exhibit stability and high dye adsorption performance in water with acidic and neutral conditions (pH range of 2 to 7) owing to its

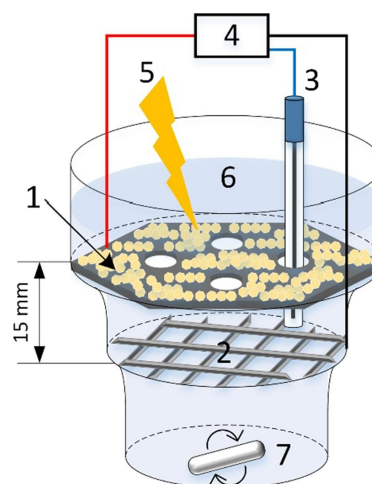


**Figure 1:** Schematic representation of the photoelectrocatalytic cell (working volume: 75 mL). (1) MOF/GP working electrode (active area: 9.61  $\text{cm}^2$ ), (2) Pt/Ti mesh counter electrode, (3) Ag/AgCl reference electrode, (4) potentiostat, (5) light source, (6) electrolyte (0.1 M phosphate buffer, pH 7.2), (7) magnetic stirring.

structured formed by 12-connected  $\text{Zr}_6$  clusters and *S. aureus* is capable to grow in a range of pH 4.0–10.0 with an optimum of 6.0–7.0, the isotonic and non-toxic 0.1 M phosphate buffer (pH 7.2) was used as electrolyte to provide a stable environment [42–44].

Disinfection runs were performed in electrocatalytic (EC, bias potential only), photocatalytic (PC, irradiation only), and photoelectrocatalytic (PEC, bias potential + irradiation) conditions. The external potential bias was set at +1.0 V vs. Ag/AgCl and Chronoamperometry (CA) curves were recorded during EC and PEC treatments. The cell was irradiated using (i) solar (Heraeus TQ Xe 150 Xe-arc lamp, 150  $\text{W m}^{-2}$ ), (ii) visible (Heraeus TQ Xe-arc lamp with R3114 UV filter, <3% transmission for light <400 nm, 150  $\text{W m}^{-2}$ ), (iii) 365 nm UVA (Mightex LED BLS 13000 $^{-1}$ , 150  $\text{W m}^{-2}$ ) and (iv) 365 nm UVA(++) (Mightex LED BLS 13000 $^{-1}$ , 2500  $\text{W m}^{-2}$ ) light irradiation. The emission spectra (Figure S1) and irradiance of the light sources were measured with a StellarNet BLUE-Wave Spectrometer.

The experiments were conducted for 60 min and the number of viable bacteria was measured at predetermined time intervals (0, 5, 10, 20, 40 and 60 min) using the plate counting method according to the standard ISO 22196. Briefly, 0.2 mL aliquots were collected from the bacterial reaction suspension and serially 10-fold diluted using phosphate-buffered saline (PBS) solution. 10  $\mu\text{L}$  drops of each dilution were placed in triplicate on agar plates (2.5  $\text{g L}^{-1}$  yeast extract, 5  $\text{g L}^{-1}$  tryptone, 1  $\text{g L}^{-1}$  glucose, 15  $\text{g L}^{-1}$  agar powder), which were incubated at 37 °C for 24 h before counting CFUs. The results are the average of two replicates with at least two serial dilutions.

The integrity and stability of the MOF-functionalized anodes was evaluated by SEM (Zeiss DSM 950). After each disinfection run, the working electrodes were removed from the reactor and submitted to a fixation process for 1 h with glutaraldehyde 5% (v/v) in 0.2 M sodium cacodylate buffer at pH 7.2, followed by dehydration with ethanol and acetone. The surfaces were gold-sputtered prior to observation.

### 3. Results and discussion

#### 3.1 MOFs properties

The crystalline structure of Zr-NDC MOF was obtained from the Cambridge Crystallographic Data Centre database (Deposition number: 1956175) and displayed in Fig. 2a [45]. The structural topology of this material is similar to that described for UiO-66(Zr), and consists of  $Zr_6O_4(OH)_4$  metal clusters interconnected through twelve NDC linkers to form a 3D periodic structure with octahedral cages ( $\sim 14$  Å) surrounded by eight tetrahedral cages ( $\sim 11$  Å) [46-49]. As shown in Fig. 2b, the experimental Zr-NDC X-ray diffractogram was consistent with the simulated one, obtained using Mercury 4.3.0 software (built around the Cambridge Structural Database, CSD), and previous reports [49,50]. The presence of two amino groups in the linker led to the formation of an isorecticular MOF, as indicated by the obtained diffraction pattern, meaning that the framework structure was formed.

Chemical stability of MOFs is essential for photoelectrocatalysis since reactions take place in aqueous

electrolyte. For that reason, the concentration of Zr(IV) ions released from the photocatalytic powders into Milli-Q water at 37 °C was measured. Zr(IV) soluble ions were below detection limit ( $1 \text{ ng L}^{-1}$ ) confirming the excellent stability of these Zr-based MOFs in water, in agreement with previous studies [49].

FTIR spectroscopy of Zr-NDC and Zr-NDC-2NH<sub>2</sub> was performed to further prove the successful functionalization of the NDC ligand in Zr-NDC-2NH<sub>2</sub> (Fig. 3). Both samples exhibited similar peaks at 1360 and 1610  $\text{cm}^{-1}$ , which belonged to C=C and C=O stretching of the organic linkers in the MOFs, respectively [51]. Likewise, the peaks appeared at around 1420 and 1570  $\text{cm}^{-1}$  were attributed to the carboxylate groups (O-C-O) in the ligand [30]. The peaks at around 550, 640, 780  $\text{cm}^{-1}$  were ascribed to the triplet of Zr-O<sub>2</sub> [30]. Compared with the FTIR spectrum of Zr-NDC, new peaks at 3450 and 3350  $\text{cm}^{-1}$  were observed for Zr-NDC-2NH<sub>2</sub>, corresponding to the asymmetrical and symmetrical stretching vibration of the amine groups of the ligand functionality [52], [53]. Moreover, Zr-NDC-2NH<sub>2</sub> spectrum displayed two weak peaks around 1640 and 1246  $\text{cm}^{-1}$ , which were associated with N-H bending vibration and C-N stretching vibration of aromatic amines, respectively [48, 54]. Therefore, FTIR results confirmed that amine functionalization in Zr-NDC-2NH<sub>2</sub> was achieved and the structure remained unchanged, in agreement with the obtained XRD patterns.

The optical properties of Zr-NDC and Zr-NDC-2NH<sub>2</sub> were investigated by UV-Vis DRS and PL spectroscopy. The results are shown in Fig. 4. Both solids showed a different absorption shape, Zr-NDC pre-

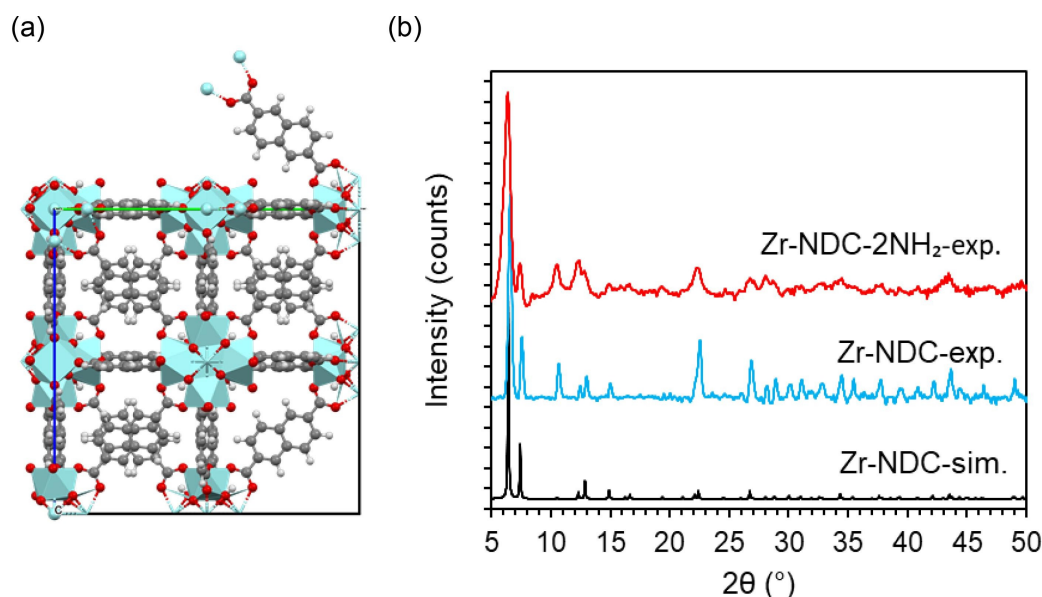


**Figure 2:** Crystalline structure of Zr-NDC (Zr polyhedral, blue; H, white; C, grey; O, red) (a) and X-ray diffraction patterns of simulated Zr-NDC (black), experimental Zr-NDC (blue) and experimental Zr-NDC-2NH<sub>2</sub> (red) (b).

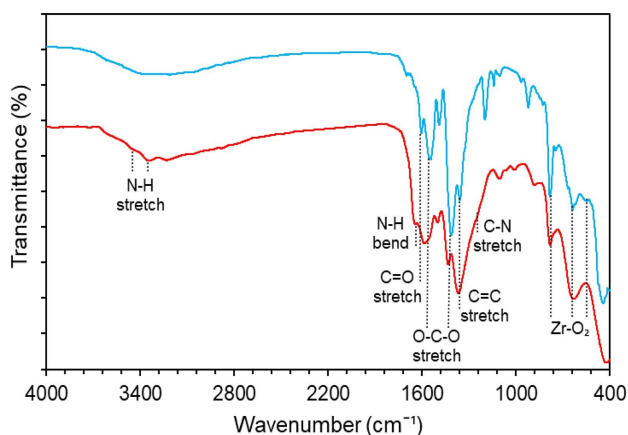


**Figure 3:** FTIR spectra of Zr-NDC (blue) and Zr-NDC-2NH<sub>2</sub> (red) (b).

sented mostly UVA absorption, with an edge located at approximately 400 nm, while Zr-NDC-2NH<sub>2</sub> exhibited wider absorption range (200–600 nm) with maximum in the UVC and, overall, higher intensity. The band gap values calculated according to the Planck-Einstein relation were 3.13 and 2.11 eV for Zr-NDC and Zr-NDC-2NH<sub>2</sub>, respectively. This band gap decrease has been previously reported [49, 55] and related to the larger electron redistribution derived from the attachment of –NH<sub>2</sub> electron-donating groups to the NDC linker.

The absorption bands of Zr-NDC could be related to the linker states. Specifically, the two bands at 365 and 300 nm can be ascribed to the (S<sub>0</sub> → S<sub>1</sub>) and (S<sub>0</sub> → S<sub>2</sub>) transitions in the  $\pi$ -conjugated naphthalene system, respectively [46]. The significantly enhanced absorption in visible light region observed with the incorporation of two –NH<sub>2</sub> groups to the linker can be attributed to the introduction of a filled band with the N 2p electrons of the NDC-2NH<sub>2</sub> linker [56].

Regarding photoluminescence, upon excitation at 365 nm (3.40 eV), the emission spectrum of Zr-NDC displayed an unique and well defined red-shifted band at 425 nm (2.92 eV) similar to that previously reported [46, 55, 57] and assigned to excimer formation due to the electronic coupling of neighboring naphthalene ligands [49, 57, 58]. Contrarily, the formation of the excimer seems to decrease the emission of Zr-NDC-2NH<sub>2</sub>, which consisted of a two-third lower intensity doublet located at minor energy (2.25–2.15 eV, 550–575 nm, respectively) than that of Zr-NDC. The excitation at longer wavelengths showed the same emission spectra for Zr-NDC while no response was obtained by Zr-NDC-2NH<sub>2</sub> indicating no activation of NDC-2NH<sub>2</sub> linkers. Meanwhile, the excitation spectra of Zr-NDC and Zr-NDC-2NH<sub>2</sub>, kept unaltered at the different emission wavelengths, which can be explained by a common ground-state origin (S<sub>0</sub>) of the emitters [57].

### 3.2 Characteristics of MOF-based anodes

MOF particle size and film thickness influence the diffusion of photoexcited electrons from the photocatalyst surface to the conductive substrate and, therefore, determine the development of the potential gradient [59]. Nanostructured electrodes with high surface roughness, such as vertically aligned TiO<sub>2</sub> nanotube array films, have been reported to exhibit an efficient charge carrier separation and thus improved photocatalytic activity when applying an anodic bias [60]. Moreover, thin films generally exhibit a decreased charge carrier recombination despite their lower light absorption as compared to thicker films [61]. Fig. 5 shows top-view SEM images of sanded graphite paper and MOF-functionalized anodes. MOF nanoparticle aggregates were distributed over the entire surface of the GP substrate with a diameter in the submicron scale and surface density of 1.04 mg cm<sup>–2</sup>. No noticeable morphological differences were detected between Zr-NDC and Zr-NDC-2NH<sub>2</sub> MOFs.

The exploration of solar light-driven photocatalysts with high activity and stability is challenging for practical applications as UV region constitutes only 3–5% of the total solar spectrum [23, 62]. Therefore, the photoelectrochemical response of Zr-NDC and Zr-NDC-2NH<sub>2</sub> functionalized electrodes was investigated under solar, visible and 365 nm UVA light irradiation. Fig. 6a and c show LSV curves at 5 mV s<sup>–1</sup> in the 0.1 M phosphate buffer (pH 7.2) electrolyte. Both MOF-based anodes displayed anodic photocurrent (difference between current response under irradiation and in the dark) with increasing current density from 0 to +1.0 V vs. Ag/AgCl, proving that photoinduced electron-hole pairs were generated and effectively separated by anodic bias promoting photoexcited electrons from the MOF to the counter electrode (cathode) through the external circuit. It can be emphasized that higher capacitive current density (dark) was obtained in the case of Zr-NDC-2NH<sub>2</sub> MOF, probably due to an enhanced electron mobility caused by the introduction of the amino groups. To further evaluate the charge-separation efficiency of the Zr-NDC and Zr-NDC-2NH<sub>2</sub> photoanodes, the transient photocurrent response was measured under chopped light irradiation (Fig. 6b and d). A steady and reproducible photocurrent response was observed during several on–off illumination cycles (500 s), which demonstrated the high photo-stability of these Zr-MOFs. Upon irradiation, a gradual increase of photocurrent density was observed, which can be attributed to traps being filled with photogenerated charge carriers and the recombination suppression as number of filled traps increases [63]. The photocurrent density value for Zr-NDC followed the order: 365 nm UVA(++) > 365 nm UVA > solar > visible,

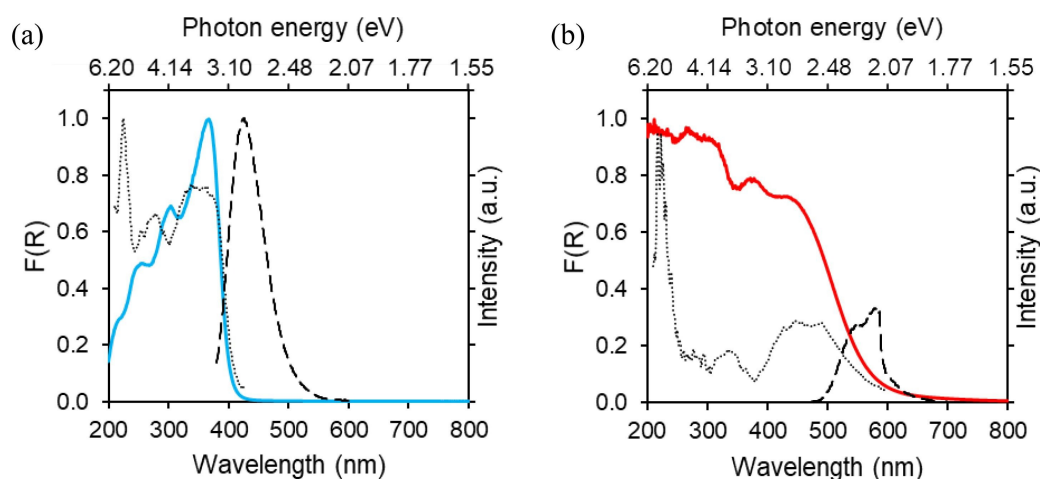


**Figure 4:** Normalized UV-vis absorption (a, blue; b, red), excitation (···) and emission (---) photoluminescence (PL) spectra of Zr-NDC (a) and Zr-NDC-2NH<sub>2</sub> (b). For emission spectra, the excitation wavelength was 365 nm.

in agreement with the UV-Vis absorption, excitation PL spectra, and photocurrents obtained from LSV measurements. On the other hand, Zr-NDC-2NH<sub>2</sub> displayed higher photocurrent density under solar and visible light irradiation but lower under UVA compared to Zr-NDC. The lower photocurrent value obtained for Zr-NDC-2NH<sub>2</sub> under 365 nm UVA illumination can be explained by the possible slowing down of the charge transfer process in this MOF as suggested by the diminished PL signal due to electron injection from -2NH<sub>2</sub> to NDC linkers [55]. As can be seen, the presence of high energy photons from UV light in the solar spectrum significantly improved photocurrent in comparison to visible light irradiation; likewise the higher UV light intensity dose, UVA(++), also led to an increment of the photocurrent value.

### 3.3 Disinfection performance

The photoelectrocatalytic disinfection performance of Zr-NDC and Zr-NDC-2NH<sub>2</sub> anodes was assessed against *S. aureus* and the logarithmic inactivation efficiency during 60 min exposure is shown in Fig.

7a-d. Likewise, photolytic experiments were carried out, leading to neglected bactericidal activity and  $\sim 2.5$ -log reduction within 60 min for 365 nm UVA and solar light irradiation, respectively (Figure S2). Both MOF-based anodes did not exhibit CFU reduction in darkness, even at the anodic bias potential of +1.0 V vs. Ag/AgCl (electrocatalytic treatment, EC) within 60 min. Moreover, the bactericidal reaction was also insignificant under visible light irradiation in all cases despite the apparent absorbance of Zr-NDC-2NH<sub>2</sub>, which correlated with the low photocurrent density obtained. In contrast, although negligible inactivation of *S. aureus* was obtained under 365 nm UVA irradiation for PC treatments, >99.7% inhibition ( $\sim 2.6$ -log reduction) for Zr-NDC and >99.4% inhibition ( $\sim 2.2$ -log reduction) for Zr-NDC-2NH<sub>2</sub> were achieved within 60 min for PEC disinfection process regardless of UV light intensity. As can be observed, complete disinfection was reached after 60 min of PC treatment under solar light irradiation for Zr-NDC-2NH<sub>2</sub> electrode. Zr-NDC exhibited similar PC disinfection activity under solar illumination, exceeding that obtained under 365 nm irradiation despite its lower photocurrent

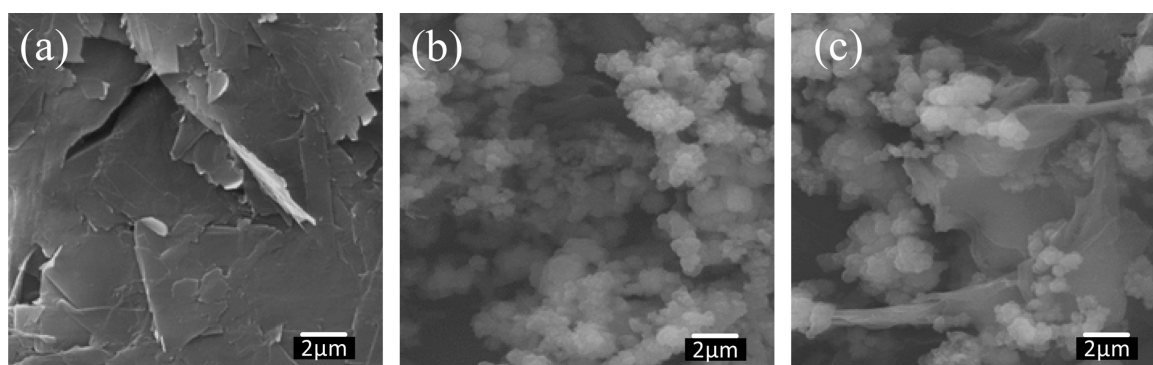


**Figure 5:** SEM images of sanded graphite paper (a), Zr-NDC (b) and Zr-NDC-2NH<sub>2</sub> (c) functionalized anodes.

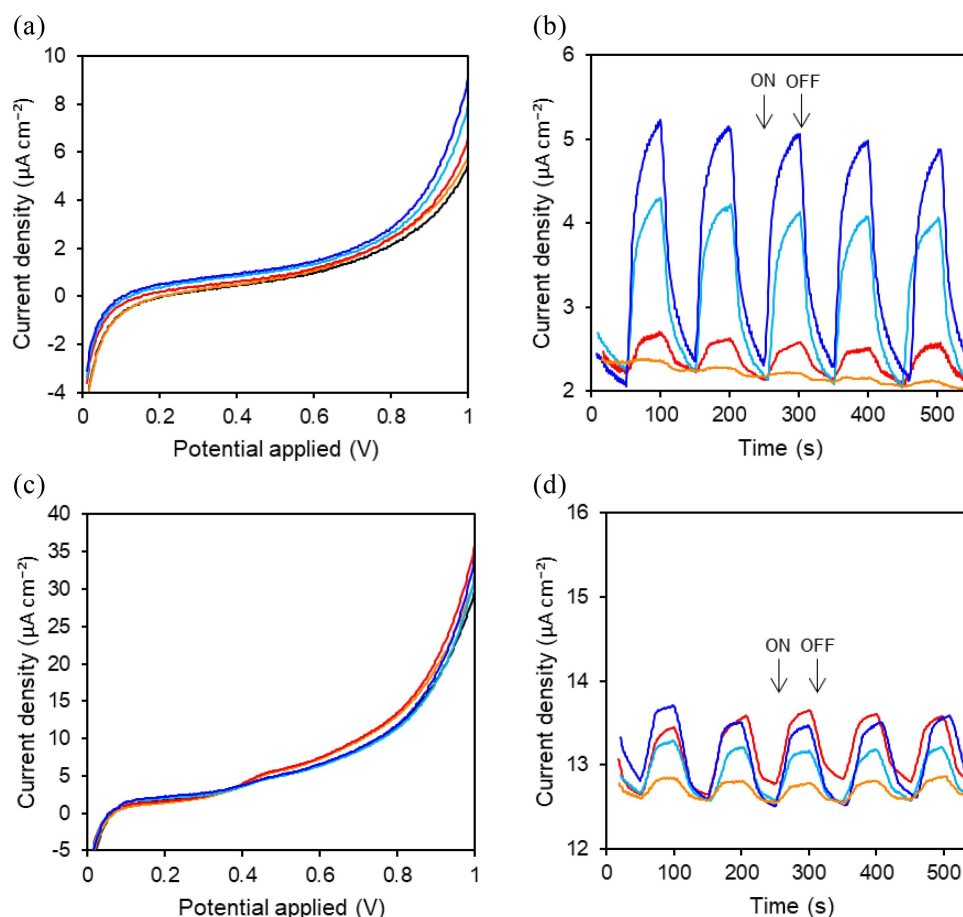


**Figure 6:** Linear sweep voltammetry (LSV) curves at  $5 \text{ mV s}^{-1}$  and transient photocurrent (TPC) responses at  $+1.0 \text{ V vs. Ag/AgCl}$  of Zr-NDC (a, b) and Zr-NDC-2NH<sub>2</sub> (c, d) anodes in  $0.1 \text{ M}$  phosphate buffer ( $\text{pH } 7.2$ ) in the absence of irradiation (black) and in the presence of visible (yellow), solar (red),  $365 \text{ nm}$  UVA (light blue), and  $365 \text{ nm}$  UVA(++) (dark blue) irradiation. The fifth LSV scan is displayed.

under full-spectrum irradiation and its lower visible light absorption. The best results were obtained for PEC treatment under solar light irradiation, reaching complete inactivation after only 20 min using either Zr-NDC or Zr-NDC-2NH<sub>2</sub> functionalized photoanodes. Therefore, PEC disinfection outperformed PC and EC processes, suggesting that the anodic bias potential effectively minimized the recombination of the photogenerated electron-hole pairs upgrading ROS production [17, 20]. CA curves were recorded during PEC disinfection treatments at  $+1.0 \text{ V vs. Ag/AgCl}$  for Zr-NDC and Zr-NDC-2NH<sub>2</sub> anodes in  $0.1 \text{ M}$  phosphate buffer (Figure S3). In accordance with LSV and TPC results, Zr-NDC exhibited a stable photocurrent response following the order:  $365 \text{ nm UVA(++)} > 365 \text{ nm UVA} > \text{solar} > \text{visible}$ . Zr-NDC-2NH<sub>2</sub> displayed a considerably higher current density and with a slight tendency to decrease during solar and UV irradiated runs.

The structure stability and integrity of active films was studied using SEM images of Zr-NDC and Zr-NDC-2NH<sub>2</sub> electrodes after PC and PEC disinfection treatments in dark conditions and in the presence of

visible, solar and  $365 \text{ nm}$  UVA light irradiation (Figure S4). A comparison is provided with the original functionalized electrodes that showed no apparent morphological differences, thereby demonstrating structural stability of the electrodes.

MOFs are known to keep some characteristics of inorganic semiconductors and some of molecular catalysts. Under irradiation MOFs undergo electronic transitions upon promotion of photoexcited electrons, but rather than a transference between delocalized valence and conduction bands, the electrons are promoted from the highest occupied crystal orbital (HOCO) to the lowest unoccupied crystal orbital (LUCO). These orbitals present different contributions from linker and node states. For the particular case of Zr-MOFs with the structure of UiO-66(Zr), the charge transfer from linker to node is relatively inefficient due to the poor overlap between the empty d-states in  $\text{Zr}_6\text{O}_4(\text{OH})_4$  cluster nodes, and the  $\pi^*$ -orbital of the ligand [64, 65]. The consequence is a gap of  $\sim 1 \text{ eV}$  between the excited linker states and the energy required for an effective LCCT [66]. Therefore, the energy required for LCCT would not

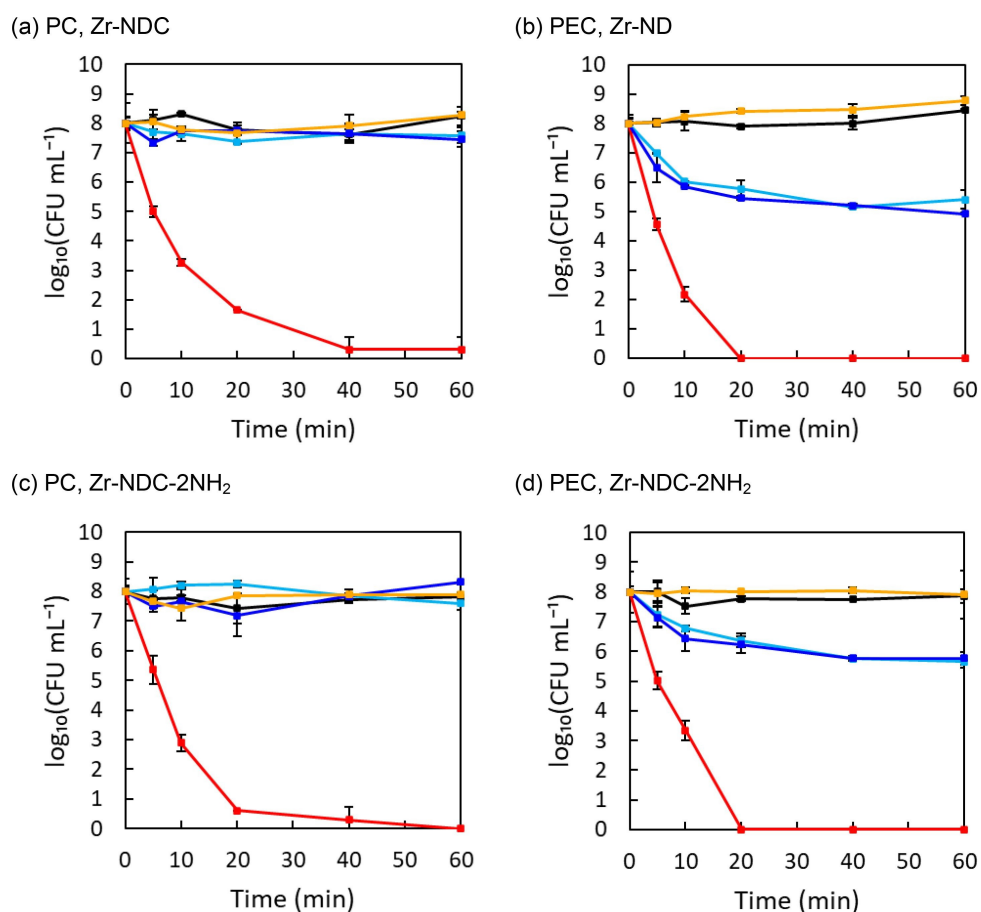


**Figure 7:** Colony-forming units (CFU) reduction of *S. aureus* for photocatalytic (PC) and photoelectrocatalytic (PEC, +1.0 V vs. Ag/AgCl) disinfection treatments using Zr-NDC (a, b) and Zr-NDC-2NH<sub>2</sub> (c, d) anodes in 0.1 M phosphate buffer (pH 7.2) in the absence of irradiation (black) and in the presence of visible (yellow), solar (red), 365 nm UVA (light blue), and 365 nm UVA(++) (dark blue) irradiation.

be accessible to 365 nm UVA irradiation in PC runs, and would require higher energy photons, that are only provided by the UVB part of the Xe-arc lamp with solar spectrum (see Figure S1). The irradiation with 365 nm was capable to reduce over two orders of magnitude ( $>2\text{-log}$  or  $>99\%$ ) the number of viable CFU, but only when working in PEC mode because in this case the bias applied reduced the energy required for LCCT. Noteworthy, the filter retaining wavelengths  $<400$  nm leads a visible radiation without disinfection activity, either in PC or PEC modes (see Fig. 7). Zr-NDC has been known to exhibit photoinduced LCCT with electrons and holes generation upon excitation with 355 nm photons [41, 55]. In this process, the organic linker acts as photoantennae that activate the metal cluster, which would receive the photogenerated electrons [67].

Increasing the  $\pi$ -conjugation by adding aromatic rings to the ligand backbones has demonstrated to enhance the optical response of MOFs due to an effective charge transfer been related to a resonance effect [38]. A band gap reduction from 4 eV to 3.3 eV was achieved by replacing BDCs in

MOF-5 with 1,4-naphthalenedicarboxylic acid and 2,6-naphthalenedicarboxylic acid [68]. In the current study, replacing BDCs in UiO-66 with more conjugated NDCs has reduced the band gap from 3.78 eV to 3.13 eV (Figure S5 a), confirming the positive effect of additional  $\pi$ -conjugation. Moreover, as displayed in Figure S5 b, this replacement not only led to an increased light absorption, but also improved the photocatalytic performance towards disinfection under solar light irradiation. Nevertheless, the inclusion of amino groups in the linker leads to higher photocurrent under solar light irradiation but does not improve the disinfection performance of PC and PEC processes. BET surface area and pore size of Zr-NDC have been previously reported to be  $1340\text{--}1720\text{ m}^2\text{ g}^{-1}$  and  $0.53\text{--}0.67\text{ cm}^3\text{ g}^{-1}$ , respectively [47–49]. The incorporation of a single amino group to the ligand in Zr-NDC-NH<sub>2</sub> decreased BET surface area from  $1340.0$  to  $1054\text{ m}^2\text{ g}^{-1}$  [48]. It is clear that the surface area and the inherent porosity of Zr-NDC diminish as the number of functional groups increases, so it is expected to be lower for Zr-NDC-2NH<sub>2</sub>. Zr-NDC-2NO<sub>2</sub> and Zr-NDC-2SO<sub>3</sub>H exhibited a decreased BET

surface area of  $812 \text{ m}^2 \text{ g}^{-1}$  and  $702 \text{ m}^2 \text{ g}^{-1}$ , respectively, as compared to the  $1392 \text{ m}^2 \text{ g}^{-1}$  obtained for Zr-NDC [47]. Although the lower surface area of Zr-NDC-NH<sub>2</sub> may provide less catalytic sites, it should be noted that amine groups would increase surface charge positivity and, thus, the interaction between the catalyst and the negatively charged bacteria, balancing the disinfection performance [69]. Therefore, this result might be due to the limited collaborative mechanism of electron injection from -NH<sub>2</sub> to NDC [55], combined with a possible higher recombination rate after the inclusion of a new HOCO state due to the amine group with higher energy and, thus, the lower oxidative potential of this new HOCO state in the organic linker of Zr-NDC-2NH<sub>2</sub> [65]. This study agrees with the LCCT mechanism in which the photoinduced electron-hole pairs leads to the generation of ROS. Specifically, the energy of the upper states of UiO-66, which corresponds to the cluster nodes, is located at about -0.53 V vs. NHE, which is enough to reduce dissolved oxygen to superoxide radical anion [70].

## 4. Conclusions

Isorecticular Zr-based MOFs were successfully synthesized using NDC (2,6-naphthalenedicarboxylic acid) and 2NH<sub>2</sub>-functionalized NDC (4,8-diaminonaphthalene-2,6-dicarboxylic acid) as organic linkers, as confirmed by XRD and FTIR analyses. MOF-based electrodes were fabricated by spray-coating onto graphite paper, achieving homogeneous layer with  $1.04 \text{ mg cm}^{-2}$ , which consisted of aggregates with diameter in the submicron scale. The excellent water-stability of the MOFs and the integrity of the as-prepared electrodes were demonstrated by IPC-AES and SEM measurements.

These catalytic electrodes were studied in PC and PEC processes. LSV and TPC measurements were conducted under solar (Xe-arc lamp), visible (Xe-arc lamp with <400 nm cut-off filter) and 365 nm LED-UVA irradiation, showing that photoinduced electron-hole pairs were generated and effectively separated. As compared to Zr-NDC, Zr-NDC-2NH<sub>2</sub> displayed higher photocurrent density under solar irradiation. The relatively low photocurrent under 365 nm UVA, could be attributed to the lower excitation capacity, insufficient electron transfer in the linkers, and a faster charge carrier recombination.

The disinfection performance of the MOF-functionalized anodes was assessed against *S. aureus* in EC, PC and PEC conditions. The bactericidal reaction was insignificant for EC and the processes carried out under visible light irradiation. Negligible inactivation was also obtained under 365 nm UVA

irradiation for PC treatments, but > 99.7% inhibition was observed for Zr-NDC and > 99.4% for of Zr-NDC-2NH<sub>2</sub> after 60 min in PEC treatments. The disinfection performance was very high for PC and PEC processes performed under solar irradiation, which contained small contribution of wavelengths < 350 nm.

The improved activity obtained under 365 nm UVA in PEC and the high disinfection capacity (up to 8-log in 20 min) observed in PC and PEC processes under solar irradiation were attributed to the enhancement of LCCT process due to high energy UVB photons, which would be capable of exciting electrons to the Zr6-oxo cluster. The incorporation of -NH<sub>2</sub> groups to the linker had no effect on PC and PEC activity towards disinfection despite the increased visible light absorption and photocurrent. This work provides a better understanding of the behaviour of Zr-based MOFs as photocatalysts and photoelectrocatalysts and demonstrates their potential use for solar disinfection processes.

## Acknowledgements

LV thanks the Spanish Ministry of Education for the FPU grant FPU17/03096. CIE acknowledges the funding from the European Union's Horizon 2020 research and innovation programme under the Marie Skłodowska-Curie grant agreement No. 754382.

## References

1. L.K. Dhandole, S.-G. Kim, Y.-S. Seo, M.A. Mahadik, H.S. Chung, S.Y. Lee, S.H. Choi, M. Cho, J. Ryu, J.S. Jang. Enhanced Photocatalytic Degradation of Organic Pollutants and Inactivation of *Listeria monocytogenes* by Visible Light Active Rh-Sb Codoped TiO<sub>2</sub> Nanorods. *ACS Sustainable Chem. Eng.*, 6 (2018), pp. 4302-4315.
2. J. He, A. Kumar, M. Khan, I.M.C. Lo. Critical review of photocatalytic disinfection of bacteria: from noble metals- and carbon nanomaterials-TiO<sub>2</sub> composites to challenges of water characteristics and strategic solutions. *Sci. Total Environ.*, 758 (2021), p. 143953.
3. A. Iftikhar, M.S. Khan, U. Rashid, Q. Mahmood, H. Zafar, M. Bilal, N. Riaz. Influence of metallic species for efficient photocatalytic water disinfection: bactericidal mechanism of in vitro results using docking simulation. *Environ. Sci. Pollut. Res.*, 27 (32) (2020), pp. 39819-39831.
4. P. Murugesan, J.A. Moses, C. Anandharamakrishnan. Photocatalytic disinfection efficiency of 2D structure graphitic carbon nitride-based nanocomposites: a review. *J. Mater. Sci.*, 54 (19) (2019), pp. 12206-12235.

5. W. Wang, C. Zhou, Y. Yang, G. Zeng, C. Zhang, Y. Zhou, J. Yang, D. Huang, H. Wang, W. Xiong, X. Li, Y. Fu, Z. Wang, Q. He, M. Jia, H. Luo. Carbon nitride based photocatalysts for solar photocatalytic disinfection, can we go further? *Chem. Eng. J.*, 404 (2021), p. 126540.
6. J.D. García-Espinoza, I. Robles, A. Durán-Moreno, L.A. Godínez. Photo-assisted electrochemical advanced oxidation processes for the disinfection of aqueous solutions: A review. *Chemosphere*, 274 (2021), p. 129957.
7. M.-T. Guo, C. Kong. Antibiotic resistant bacteria survived from UV disinfection: Safety concerns on genes dissemination. *Chemosphere*, 224 (2019), pp. 827-832.
8. Q. Zhao, N. Li, C. Liao, L. Tian, J. An, X. Wang. The UV/H<sub>2</sub>O<sub>2</sub> process based on H<sub>2</sub>O<sub>2</sub> in-situ generation for water disinfection. *J. Hazard. Mater. Lett.*, 2 (2021), p. 100020.
9. S. Ghasemian, B. Asadishad, S. Omanovic, N. Tufenkji. Electrochemical disinfection of bacteria-laden water using antimony-doped tungsten-oxide electrodes. *Water Res.*, 126 (2017), pp. 299-307.
10. J. Byrne, P. Dunlop, J. Hamilton, P. Fernández-Ibáñez, I. Polo-López, P. Sharma, A. Vennard. A Review of Heterogeneous Photocatalysis for Water and Surface Disinfection. *Molecules*, 20 (4) (2015), pp. 5574-5615.
11. A. Habibi-Yangjeh, S. Asadzadeh-Khaneghah, S. Feizpoor, A. Rouhi. Review on heterogeneous photocatalytic disinfection of waterborne, airborne, and foodborne viruses: Can we win against pathogenic viruses? *J. Colloid Interface Sci.*, 580 (2020), pp. 503-514.
12. L. Valenzuela, A. Iglesias, M. Faraldos, A. Bahamonde, R. Rosal. Antimicrobial surfaces with self-cleaning properties functionalized by photocatalytic ZnO electrospayed coatings. *J. Hazard. Mater.*, 369 (2019), pp. 665-673.
13. H. Yan, R. Wang, RuiXi Liu, T. Xu, J. Sun, L. Liu, J. Wang. Recyclable and reusable direct Z-scheme heterojunction CeO<sub>2</sub>/TiO<sub>2</sub> nanotube arrays for photocatalytic water disinfection. *Appl. Catal. B*, 291 (2021), p. 120096.
14. B. Ezraty, A. Gennaris, F. Barras, J.-F. Collet. Oxidative stress, protein damage and repair in bacteria *Nat. Rev. Microbiol.*, 15 (7) (2017), pp. 385-396.
15. H. Park, H.-I. Kim, G.-H. Moon, W. Choi. Photoinduced charge transfer processes in solar photocatalysis based on modified TiO<sub>2</sub>. *Energy Environ. Sci.*, 9 (2) (2016), pp. 411-433.
16. R.B. Domínguez-Espíndola, C. Bruguera-Casamada, S. Silva-Martínez, R.M. Araujo, E. Brillas, I. Sirés. Photoelectrocatalytic inactivation of *Pseudomonas aeruginosa* using an Ag-decorated TiO<sub>2</sub> photoanode. *Sep. Purif. Technol.*, 208 (2019), pp. 83-91,
17. S. McMichael, M. Waso, B. Reyneke, W. Khan, J.A. Byrne, P. Fernandez-Ibanez. Electrochemically assisted photocatalysis for the disinfection of rainwater under solar irradiation. *Appl. Catal. B*, 281 (2021), p. 119485.
18. S.-F. Su, L.-M. Ye, Q.-M. Tian, W.-B. Situ, X.-L. Song, S.-Y. Ye. Photoelectrocatalytic inactivation of *Penicillium expansum* spores on a Pt decorated TiO<sub>2</sub>/activated carbon fiber photoelectrode in an all-solid-state photoelectrochemical cell. *Appl. Surf. Sci.*, 515 (2020), p. 145964.
19. S. Hand, R.D. Cusick. Electrochemical Disinfection in Water and Wastewater Treatment: Identifying Impacts of Water Quality and Operating Conditions on Performance. *Environ. Sci. Technol.*, 55 (6) (2021), pp. 3470-3482.
20. K. Cho, S. Lee, H. Kim, H.-E. Kim, A. Son, E.-j. Kim, M. Li, Z. Qiang, S.W. Hong. Effects of reactive oxidants generation and capacitance on photoelectrochemical water disinfection with self-doped titanium dioxide nanotube arrays. *Appl. Catal. B*, 257 (2019), p. 117910.
21. Z. Gu, X. An, H. Lan, Y. Tian, J. Zhang, R. Liu, H. Liu, J. Qu. Microfluidic-enhanced 3-D photoanodes with free interfacial energy barrier for photoelectrochemical applications. *Appl. Catal. B*, 244 (2019), pp. 740-747.
22. P. Mazierski, A.F. Borzyszkowska, P. Wilczewska, A. Białk-Bielińska, A. Zaleska-Medynska, E.M. Siedlecka, A. Pieczyńska. Removal of 5-fluorouracil by solar-driven photoelectrocatalytic oxidation using Ti/TiO<sub>2</sub>(NT) photoelectrodes. *Water Res.*, 157 (2019), pp. 610-620.
23. Q. Wang, Q. Gao, A.M. Al-Enizi, A. Nafady, S. Ma. Recent advances in MOF-based photocatalysis: environmental remediation under visible light. *Inorg. Chem. Front.*, 7 (2) (2020), pp. 300-339.
24. Y. Wang, M. Zhao, C. Hou, W. Chen, S. Li, R. Ren, Z. Li. Efficient degradation of perfluorooctanoic acid by solar photo-electro-Fenton like system fabricated by MOFs/carbon nanofibers composite membrane. *Chem. Eng. J.*, 414 (2021), p. 128940.
25. H.-H. Zou, W.-Q. Li, H. Zhang, L. Liu, C.-T. He, S.-L. Zhong. An unexpected broad-spectral absorbed lanthanum oxychloride and lanthanum titanate heterostructure promoted photoelectrocatalytic hydrogen evolution. *Chem. Eng. J.*, 404 (2021), p. 126567.

26. M. Nemiwal, V. Subbaramaiah, T.C. Zhang, D. Kumar. Recent advances in visible-light-driven carbon dioxide reduction by metal-organic frameworks. *Sci. Total Environ.*, 762 (2021), p. 144101.
27. X. Song, Y.u. Wang, T. Zhu, J. Liu, S. Zhang. Facile synthesis a novel core-shell amino functionalized MIL-125(Ti) micro-photocatalyst for enhanced degradation of tetracycline hydrochloride under visible light. *Chem. Eng. J.*, 416 (2021), p. 129126.
28. T. Zhang, W. Lin. Metal-organic frameworks for artificial photosynthesis and photocatalysis. *Chem. Soc. Rev.*, 43 (16) (2014), pp. 5982-5993.
29. J. An, Y. Li, W. Chen, G. Li, J. He, H. Feng. Electrochemically-deposited PANI on iron mesh-based metal-organic framework with enhanced visible-light response towards elimination of thiamphenicol and *E. coli*. *Environ. Res.*, 191 (2020), p. 110067.
30. X.i. Chen, Q. Li, J. Li, J. Chen, H. Jia. Modulating charge separation via in situ hydrothermal assembly of low content Bi<sub>2</sub>S<sub>3</sub> into UiO-66 for efficient photothermocatalytic CO<sub>2</sub> reduction. *Appl. Catal. B*, 270 (2020), p. 118915.
31. P. Li, J. Li, X. Feng, J. Li, Y. Hao, J. Zhang, H. Wang, A. Yin, J. Zhou, X. Ma, B. Wang. Metal-organic frameworks with photocatalytic bactericidal activity for integrated air cleaning. *Nat. Commun.*, 10 (1) (2019), p. 2177.
32. S. Abednatanzi, P. Gohari Derakhshandeh, H. Depauw, F.-X. Coudert, H. Vrielinck, P. Van Der Voort, K. Leus. Mixed-metal metal-organic frameworks. *Chem. Soc. Rev.*, 48 (9) (2019), pp. 2535-2565.
33. M. Kim, J.F. Cahill, H. Fei, K.A. Prather, S.M. Cohen. Postsynthetic Ligand and Cation Exchange in Robust Metal-Organic Frameworks. *J. Am. Chem. Soc.*, 134 (43) (2012), pp. 18082-18088.
34. D. Jiang, P. Xu, H. Wang, G. Zeng, D. Huang, M. Chen, C. Lai, C. Zhang, J. Wan, W. Xue. Strategies to improve metal organic frameworks photocatalyst's performance for degradation of organic pollutants. *Coord. Chem. Rev.*, 376 (2018), pp. 449-466.
35. S. Li, P. Luo, H. Wu, C. Wei, Y. Hu, G. Qiu. Strategies for Improving the Performance and Application of MOFs Photocatalysts. *ChemCatChem*, 11 (13) (2019), pp. 2978-2993.
36. P. Du, J. Schneider, P. Jarosz, R. Eisenberg. Photocatalytic Generation of Hydrogen from Water Using a Platinum(II) Terpyridyl Acetylide Chromophore. *J. Am. Chem. Soc.*, 128 (24) (2006), pp. 7726-7727.
37. Y.K. Park, S.B. Choi, H.J. Nam, D.-Y. Jung, H.C. Ahn, K. Choi, H. Furukawa, J. Kim. Catalytic nickel nanoparticles embedded in a mesoporous metal-organic framework. *Chem. Comm.*, 46 (18) (2010), pp. 3086-3088.
38. Y. Wen, P. Zhang, V.K. Sharma, X. Ma, H.-C. Zhou. Metal-organic frameworks for environmental applications. *Cell Rep. Phys. Sci.*, 2 (2) (2021), p. 100348.
39. J.H. Cavka, S. Jakobsen, U. Olsbye, N. Guillou, C. Lamberti, S. Bordiga, K.P. Lillerud. A New Zirconium Inorganic Building Brick Forming Metal Organic Frameworks with Exceptional Stability. *J. Am. Chem. Soc.*, 130 (42) (2008), pp. 13850-13851.
40. A. Kirchon, L. Feng, H.F. Drake, E.A. Joseph, H.-C. Zhou. From fundamentals to applications: a toolbox for robust and multifunctional MOF materials. *Chem. Soc. Rev.*, 47 (23) (2018), pp. 8611-8638.
41. X. Li, S. Surendran Rajasree, J. Yu, P. Deria. The role of photoinduced charge transfer for photocatalysis, photoelectrocatalysis and luminescence sensing in metal-organic frameworks. *Dalton Trans.*, 49 (37) (2020), pp. 12892-12917.
42. Y. Bai, Y. Dou, L.-H. Xie, W. Rutledge, J.-R. Li, H.-C. Zhou. Zr-based metal-organic frameworks: design, synthesis, structure, and applications. *Chem. Soc. Rev.*, 45 (8) (2016), pp. 2327-2367.
43. L.H.T. Nguyen, H.T.T. Nguyen, B.Q.G. Le, M.-H. Dang, T.T.T. Nguyen, N.X.D. Mai, T.L.H. Doan. Microwave-assisted solvothermal synthesis of defective zirconium-organic framework as a recyclable nano-adsorbent with superior adsorption capacity for efficient removal of toxic organic dyes. *Colloid Interface Sci. Commun.* (2021), p. 100511.
44. A. Valero, F. Pérez-Rodríguez, E. Carrasco, J.M. Fuentes-Alventosa, R.M. García-Gimeno, G. Zurera. Modelling the growth boundaries of *Staphylococcus aureus*: Effect of temperature, pH and water activity. *Int. J. Food Microbiol.*, 133 (1) (2009), pp. 186-194.
45. W. Zhang, H. Huang, D. Liu, Q. Yang, Y. Xiao, Q. Ma, C. Zhong. CCDC 1956175 Experimental Crystal Structure Determination (2019), 10.5517/ccdc.csd.cc23nkfs
46. M. Gutiérrez, R. Navarro, F. Sánchez, A. Douhal. Photodynamics of Zr-based MOFs: effect of explosive nitroaromatics. *Phys. Chem. Chem. Phys.*, 19 (25) (2017), pp. 16337-16347.
47. H. Huang, W. Zhang, F. Yang, B. Wang, Q. Yang, Y. Xie, C. Zhong, J.-R. Li. Enhancing CO<sub>2</sub> adsorption and separation ability of Zr(IV)-based metal-organic frameworks through ligand func-

- tionalization under the guidance of the quantitative structure–property relationship model. *Chem. Eng. J.*, 289 (2016), pp. 247-253.
48. A.M. Raseo-Almansa, A. Corma, M. Iglesias, F. Sánchez. Zirconium Materials from Mixed Dicarboxylate Linkers: Enhancing the Stability for Catalytic Applications. *ChemCatChem*, 6 (12) (2014), pp. 3426-3433.
  49. W. Zhang, H. Huang, D. Liu, Q. Yang, Y. Xiao, Q. Ma, C. Zhong. A new metal–organic framework with high stability based on zirconium for sensing small molecules. *Microporous Mesoporous Mater.*, 171 (2013), pp. 118-124.
  50. C.F. Macrae, I. Sovago, S.J. Cottrell, P.T.A. Galek, P. McCabe, E. Pidcock, M. Platings, G.P. Shields, J.S. Stevens, M. Towler, P.A. Wood. Mercury 4.0: from visualization to analysis, design and prediction. *J. Appl. Crystallogr.*, 53 (1) (2020), pp. 226-235.
  51. Z.U. Zango, N.S. Sambudi, K. Jumbri, N.H.H. Abu Bakar, N.A.F. Abdullah, E.-S. Negim, B. Saad. Experimental and molecular docking model studies for the adsorption of polycyclic aromatic hydrocarbons onto UiO-66(Zr) and NH<sub>2</sub>-UiO-66(Zr) metal-organic frameworks. *Chem. Eng. Sci.*, 220 (2020), p. 115608.
  52. L. Shen, S. Liang, W. Wu, R. Liang, L. Wu. Multifunctional NH<sub>2</sub>-mediated zirconium metal–organic framework as an efficient visible-light-driven photocatalyst for selective oxidation of alcohols and reduction of aqueous Cr(VI). *Dalton Trans.*, 42 (37) (2013), pp. 13649-13657.
  53. F. Vermoortele, R. Ameloot, A. Vimont, C. Serre, D. De Vos. An amino-modified Zr-terephthalate metal–organic framework as an acid–base catalyst for cross-aldol condensation. *Chem. Comm.*, 47 (5) (2011), pp. 1521-1523.
  54. M. Kandiah, S. Usseglio, S. Svelle, U. Olsbye, K.P. Lillerud, M. Tilset. Post-synthetic modification of the metal–organic framework compound UiO-66. *J. Mater. Chem.*, 20 (44) (2010), pp. 9848-9851.
  55. M. Gutierrez, B. Cohen, F. Sánchez, A. Douhal. Photochemistry of Zr-based MOFs: ligand-to-cluster charge transfer, energy transfer and excimer formation, what else is there? *Phys. Chem. Chem. Phys.*, 18 (40) (2016), pp. 27761-27774.
  56. A. Dhakshinamoorthy, Z. Li, H. Garcia. Catalysis and photocatalysis by metal organic frameworks. *Chem. Soc. Rev.*, 47 (22) (2018), pp. 8134-8172.
  57. M. Gutiérrez, F. Sánchez, A. Douhal. Spectral and dynamical properties of a Zr-based MOF. *Phys. Chem. Chem. Phys.*, 18 (7) (2016), pp. 5112-5120.
  58. S. Liu, Z. Xiang, Z. Hu, X. Zheng, D. Cao. Zeolitic imidazolate framework-8 as a luminescent material for the sensing of metal ions and small molecules. *J. Mater. Chem.*, 21 (18) (2011), pp. 6649-6653.
  59. C. Pablos, J. Marugán, C. Adán, M. Osuna, R. van Grieken. Performance of TiO<sub>2</sub> photoanodes toward oxidation of methanol and *E. coli* inactivation in water in a scaled-up photoelectrocatalytic reactor. *Electrochim. Acta* 258, 258 (2017), pp. 599-606.
  60. M. Zlamal, J.M. Macak, P. Schmuki, J. Krýsa. Electrochemically assisted photocatalysis on self-organized TiO<sub>2</sub> nanotubes. *Electrochem. Commun.*, 9 (12) (2007), pp. 2822-2826.
  61. R. Gutkowski, W. Schuhmann. Electrochemically induced sol–gel deposition of ZnO films on Pt-nanoparticle modified FTO surfaces for enhanced photoelectrocatalytic energy conversion. *Phys. Chem. Chem. Phys.*, 18 (16) (2016), pp. 10758-10763.
  62. B.C.e. Silva, K. Irikura, R.C.G. Frem, M.V.B. Zanoni. Effect of Cu(BDC-NH<sub>2</sub>) MOF deposited on Cu/Cu<sub>2</sub>O electrode and its better performance in photoelectrocatalytic reduction of CO<sub>2</sub>. *J. Electroanal. Chem.*, 880 (2021), p. 114856.
  63. H. Tsuchiya, J.M. Macak, A. Ghicov, A.S. Räder, L. Taveira, P. Schmuki. Characterization of electronic properties of TiO<sub>2</sub> nanotube films. *Corros. Sci.*, 49 (1) (2007), pp. 203-210.
  64. M.A. Nasalevich, C.H. Hendon, J.G. Santaclara, K. Svane, B. van der Linden, S.L. Veber, M.V. Fedin, A.J. Houtepen, M.A. van der Veen, F. Kapteijn, A. Walsh, J. Gascón. Electronic origins of photocatalytic activity in d0 metal organic frameworks *Sci. Rep.*, 6 (2016), p. 23676.
  65. K. Hendrickx, J.J. Joos, A. De Vos, D. Poelman, P.F. Smet, V. Van Speybroeck, P. Van Der Voort, K. Lejaeghere. Exploring lanthanide doping in UiO-66: a combined experimental and computational study of the electronic structure. *Inorg. Chem.*, 57 (9) (2018), pp. 5463-5474.
  66. A. De Vos, K. Hendrickx, P. Van Der Voort, V. Van Speybroeck, K. Lejaeghere. Missing linkers: an alternative pathway to UiO-66 electronic structure engineering. *Chem. Mater.*, 29 (7) (2017), pp. 3006-3019.
  67. S. Sun, Y. Xiao, L. He, Y. Tong, D. Liu, J. Zhang. Zr-based metal-organic framework films grown on bio-template for photoelectrocatalysis. *ChemistrySelect*, 5 (44) (2020), pp. 13855-13861.
  68. J. Gascón, M.D. Hernández-Alonso, A. Almeida, G.M. van Klink, F. Kapteijn, G. Mul. Isorecticular MOFs as Efficient Photocatalysts with Tunable

Band Gap: An Operando FTIR Study of the Photoinduced Oxidation of Propylene. *ChemSusChem*, 1 (12) (2008), pp. 981-983.

69. N. Ahmad, N.A.H. Md Nordin, J. Jaafar, N.A.N. Nik Malek, A.F. Ismail, M.K.N. Ramli. Modification of zeolitic imidazolate framework-8 with amine groups for improved antibacterial activity. *Mater. Today: Proc.*, 46 (2021), pp. 2024-2029.
70. X. Zhang, Y. Yang, W. Huang, Y. Yang, Y. Wang, C. He, N. Liu, M. Wu, L. Tang. g-C<sub>3</sub>N<sub>4</sub>/UiO-66 nanohybrids with enhanced photocatalytic activities for the oxidation of dye under visible light irradiation. *Mater. Res. Bull.*, 99 (2018), pp. 349-358.

# Supplementary Materials

## Zirconium-based Metal-Organic Frameworks for highly efficient solar light-driven photoelectrocatalytic disinfection

Laura Valenzuela<sup>1,\*</sup>, Georgiana Amariei<sup>2</sup>, Chizoba I. Ezugwu<sup>1</sup>, Marisol Faraldos<sup>3</sup>,  
Ana Bahamonde<sup>3</sup>, Marta E.G. Mosquera<sup>4</sup> and Roberto Rosal<sup>1</sup>

<sup>1</sup>Department of Chemical Engineering, Universidad de Alcalá, 28805 Alcalá de Henares, Madrid, Spain

<sup>2</sup>Department of Biological and Chemical Engineering-Process and Materials Engineering, Aarhus University, Denmark

<sup>3</sup>Instituto de Catálisis y Petroleoquímica, ICP-CSIC, Marie Curie 2, 28049 Madrid, Spain

<sup>4</sup>Department of Organic and Inorganic Chemistry, Institute of Chemical Research Andrés M. del Río (IQAR), Universidad de Alcalá, 28805 Alcalá de Henares, Madrid, Spain

### Contents:

**Figure S1.** Emission spectra of Heraeus TQ Xe 150 Xe-arc lamp (a), Heraeus TQ Xe-arc lamp with R3114 UV filter (b) and Mightex UV LED BLS 13000-1 (c).

**Figure S2.** Colony-forming units (CFU) reduction of *S. aureus* for photolytic disinfection treatments in 0.1M phosphate buffer (pH 7.2) conducted in the presence of working (graphite paper) and counter (Pt/Ti mesh) electrodes under solar (red) and 365 nm UVA(++) (blue) light irradiation.

**Figure S3.** Chronoamperometry (CA) curves obtained at +1.0 V vs. Ag/AgCl for Zr-NDC (a) and Zr-NDC-2NH<sub>2</sub> (b) anodes in 0.1M phosphate buffer (pH 7.2) during photoelectrocatalytic disinfection treatments in the absence of irradiation (black) and in the presence of visible (yellow), solar (red), 365 nm UVA (light blue), and 365 nm UVA(++) (dark blue) light irradiation.

**Figure S4.** SEM images of Zr-NDC and Zr-NDC-2NH<sub>2</sub> functionalized anodes after photocatalytic (PC) and photoelectrocatalytic (PEC, +1.0 V vs. Ag/AgCl) disinfection treatments in 0.1M phosphate buffer (pH 7.2) in the absence of irradiation and in the presence of visible, solar, 365 nm UVA, and 365 nm UVA(++) light irradiation.

**Figure S5.** Normalized UV-vis absorption (a) and colony-forming units (CFU) reduction of *S. aureus* for photocatalytic (PC) disinfection treatments under solar light irradiation (b) for Zr-NDC (blue) and UiO-66 (red).

---

\* Corresponding author: laura.valenzuela@uah.es

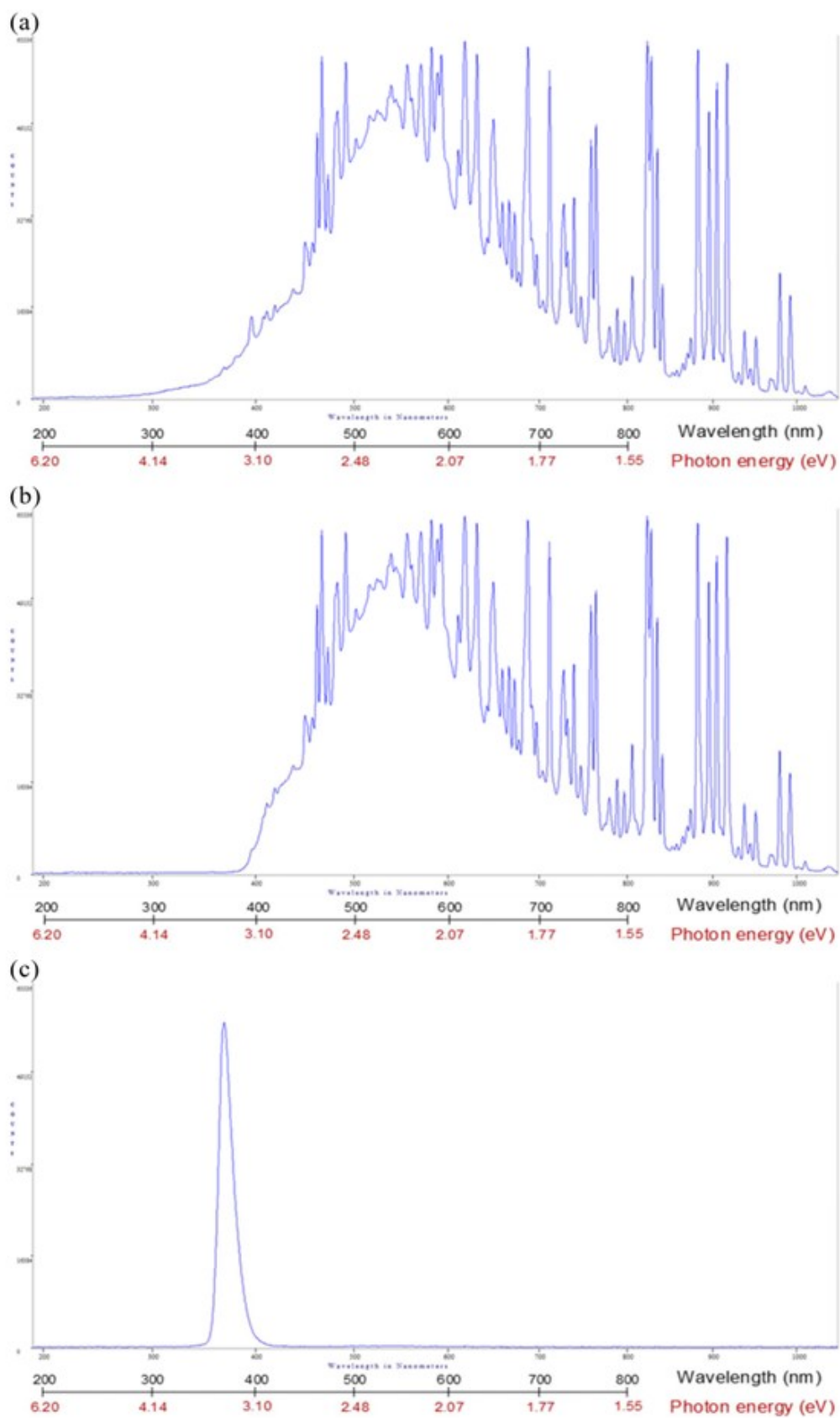


**Figure S1:** Emission spectra of Heraeus TQ Xe 150 Xe-arc lamp (a), Heraeus TQ Xe-arc lamp with R3114 UV filter (b) and Mightex UV LED BLS 13000-1 (c).

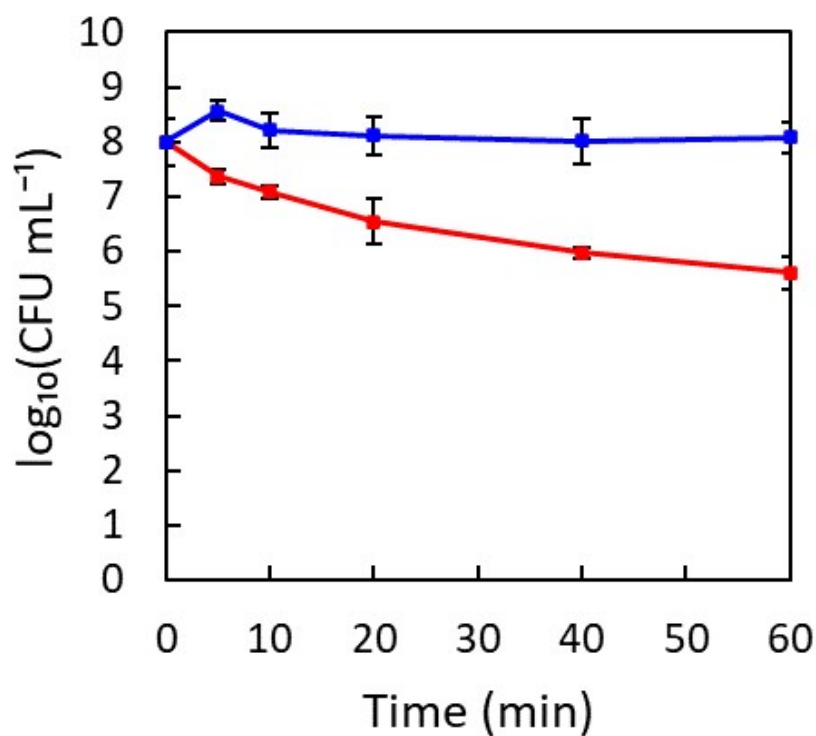


**Figure S2:** Colony-forming units (CFU) reduction of *S. aureus* for photolytic disinfection treatments in 0.1M phosphate buffer (pH 7.2) conducted in the presence of working (graphite paper) and counter (Pt/Ti mesh) electrodes under solar (red) and 365 nm UVA(++) (blue) light irradiation.

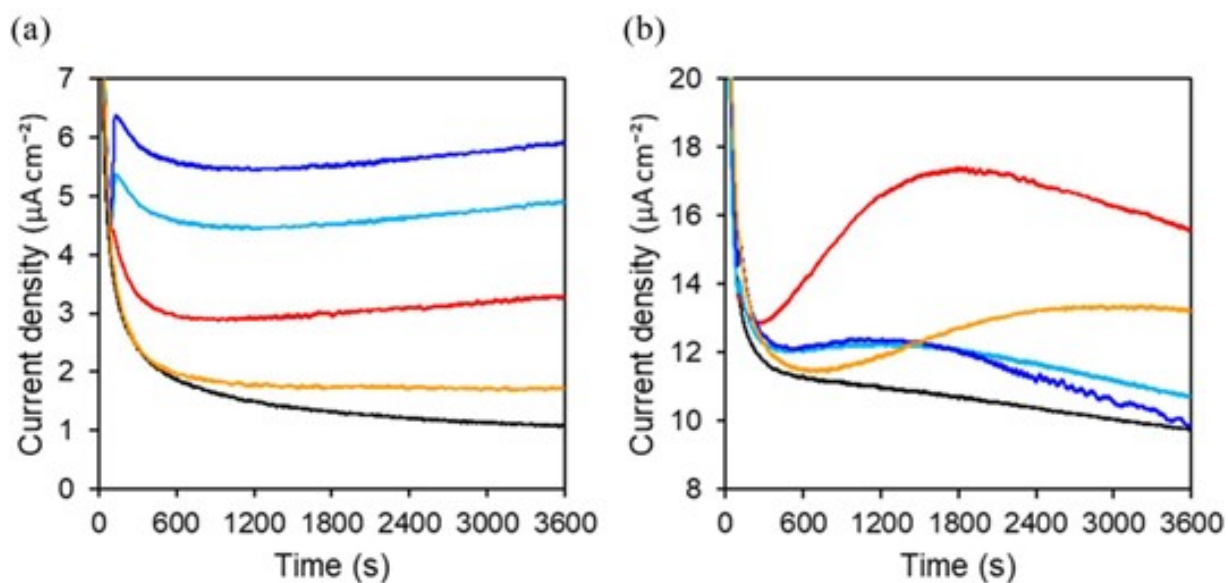


**Figure S3:** Chronoamperometry (CA) curves obtained at +1.0 V vs. Ag/AgCl for Zr-NDC (a) and Zr-NDC-2NH<sub>2</sub> (b) anodes in 0.1M phosphate buffer (pH 7.2) during photoelectrocatalytic disinfection treatments in the absence of irradiation (black) and in the presence of visible (yellow), solar (red), 365 nm UVA (light blue), and 365 nm UVA(++) (dark blue) light irradiation.

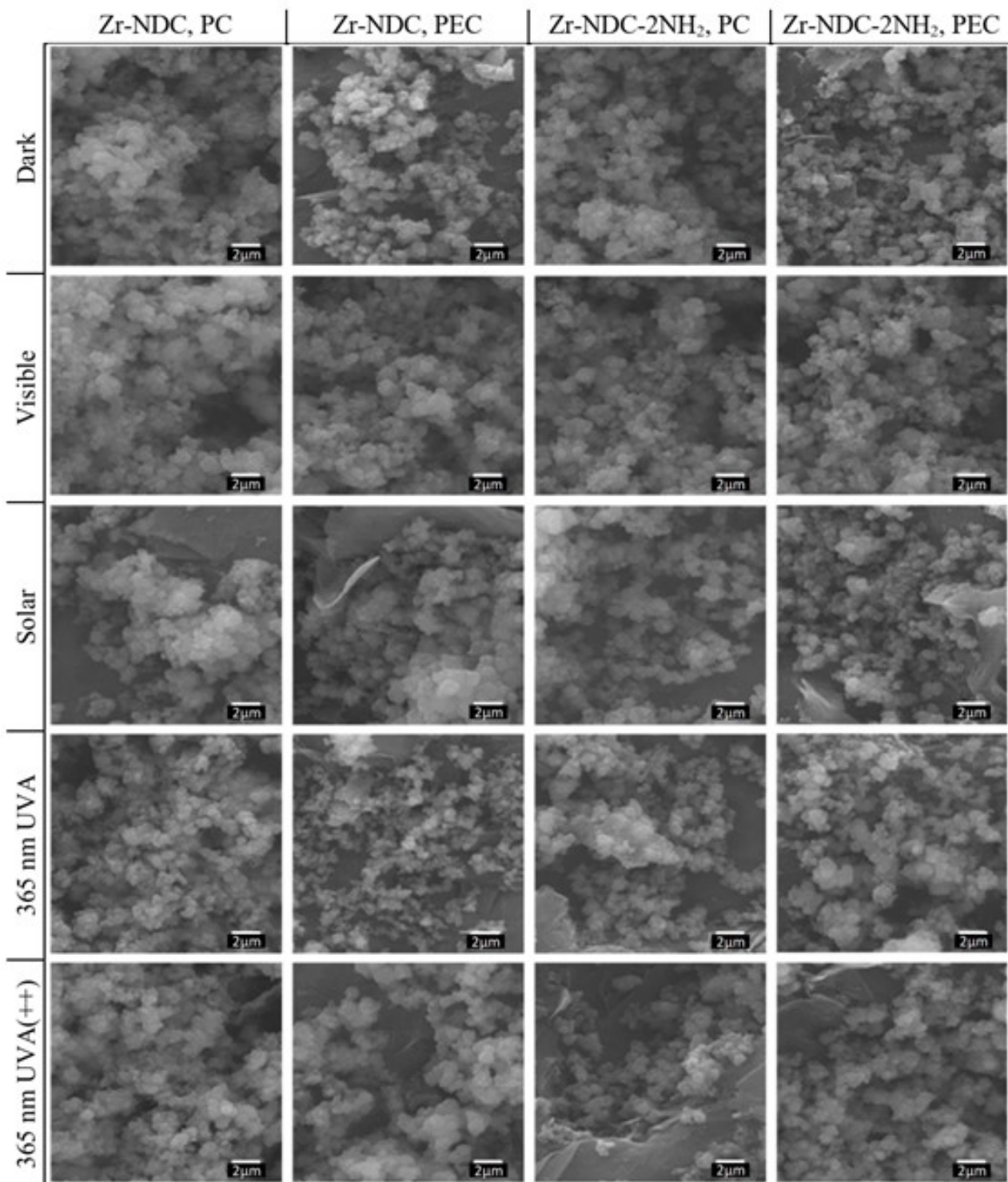


**Figure S4:** SEM images of Zr-NDC and Zr-NDC-2NH<sub>2</sub> functionalized anodes after photocatalytic (PC) and photoelectrocatalytic (PEC, +1.0 V vs. Ag/AgCl) disinfection treatments in 0.1M phosphate buffer (pH 7.2) in the absence of irradiation and in the presence of visible, solar, 365 nm UVA, and 365 nm UVA(++) light irradiation.

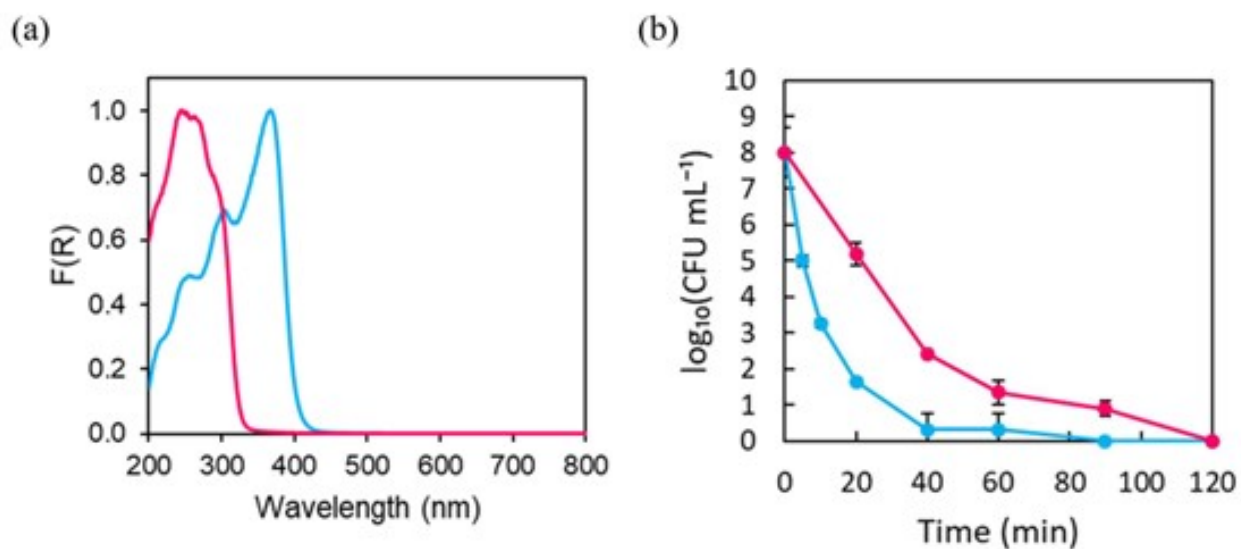


**Figure S5:** Normalized UV-vis absorption (a) and colony-forming units (CFU) reduction of *S. aureus* for photocatalytic (PC) disinfection treatments under solar light irradiation (b) for Zr-NDC (blue) and UiO-66 (red).